

Element-specific structure of materials with intrinsic disorder by high-energy resonant x-ray diffraction and differential atomic pair-distribution functions: A study of PtPd nanosized catalysts

V. Petkov^{1,*} and S. D. Shastri²¹*Department of Physics, Central Michigan University, Mt. Pleasant, Michigan 48859, USA*²*Advanced Photon Source, Argonne National Laboratory, Argonne, Illinois 60439, USA*

(Received 23 January 2010; published 21 April 2010)

We demonstrate how high-energy resonant x-ray diffraction (XRD) and differential atomic-pair-distribution function (PDF) analysis can be used to characterize the atomic ordering in materials of limited structural coherence with both excellent spatial resolution and element specificity. First we prove that this experimental approach is feasible by probing the *K*-absorption edge of Au (~81 keV) atoms in chemically ordered and disordered bulk Cu₃Au alloys. The resulting Au-differential PDFs show very clearly the different ways Au atoms are known to occupy the sites of otherwise identical cubic lattices of those materials. Next we apply it to a more complex material: PtPd alloy and core-shell nanosized (~2–4 nm) particles by probing the *K*-absorption edge of Pt (~78 keV). The resulting Pt-differential atomic PDFs reveal how exactly the atomic ordering of catalytically active Pt atoms is affected by the nanoparticles' design, thus providing a firm structural basis for understanding their properties. The work is a step forward in expanding the limits of applicability of nontraditional XRD to the rapidly growing field of materials of unusual structural complexity.

DOI: [10.1103/PhysRevB.81.165428](https://doi.org/10.1103/PhysRevB.81.165428)

PACS number(s): 61.05.cp, 61.46.Hk

I. INTRODUCTION

Many materials of current scientific and technological interest, such as crystals with local topological and/or chemical disorder, nanosized particles (NPs), glasses, and others do not exhibit a perfect long-range and periodic atomic ordering, and hence, are difficult to characterize structurally by traditional (Bragg) x-ray diffraction. This stems from the fact that when studied with x-rays, such materials act as diffraction gratings of a limited structural coherence length and, hence, produce diffraction patterns with smeared Bragg-type peaks and a diffuse component that may not be neglected. As shown recently, a combination of high-energy x-ray diffraction (XRD) with atomic-pair-distribution-function (PDF) data analysis is much better suited to the task.^{1–4} A single high-energy XRD experiment, however, yields a so-called total PDF which is a weighted sum of several contributions each reflecting the spatial correlations between a particular pair of atoms in the material. This can make difficult or ambiguous the interpretation of PDF data, especially in the case of multielement materials. Element selectivity may be added by employing spectroscopy techniques such as extended x-ray absorption fine structure spectroscopy (EXAFS) or imaging techniques such as high-angle-annular-dark-field scanning transmission electron microscopy (HAADF-STEM). The EXAFS technique is very useful but yields information on the atomic ordering extending out to 5–6 Å only. Thus, for example, an EXAFS experiment would hardly distinguish between a hexagonal (hcp) and a face-centered cubic (fcc) close packing of atoms since both show first and second coordination spheres of twelve and six atoms, respectively. Likewise, HAADF-STEM can reveal a material's morphology and compositional variations with atomic resolution. However, HAADF-STEM images, like all others, are just a projection down an axis and are not very sensitive to the atomic ordering inside materials. The difficulty may be overcome by employing the so-called resonant

XRD,⁵ which involves measuring two diffraction data sets close to but below the absorption edge of an atomic species, taking the difference between these two data sets, and Fourier transforming it into a quantity called a differential atomic PDF.^{5,6} Similarly to EXAFS, the differential PDF will reflect only correlations relative to the element whose absorption edge is probed. However, unlike EXAFS, it will show these correlations up to the longest interatomic distances to which they extend.⁷ Note, to have those correlations clearly resolved the resonant XRD data still have to be collected to sufficiently high scattering wave vectors (e.g., $q > 20 \text{ \AA}^{-1}$). This can be achieved when high-energy x-ray *K*-absorption edges of higher *Z* elements in the material of interest are probed.

Successful resonant XRD and differential atomic PDF studies on materials of limited structural coherence have already been carried out at the *K* edges of atomic species with relatively low atomic numbers *Z* ranging from 25 (Mn *K* edge ~6.5 keV) to 49 (In *K* edge ~28 keV) reaching wave vectors extending to only about 8 and 20 Å⁻¹, respectively.^{5,8} The possibility of conducting such studies using x-rays of much higher energy has been questioned so far, citing the relatively small values of the anomalous dispersion corrections to the x-ray scattering factors of heavier (higher *Z*) elements. Enabled by optimized high-energy synchrotron x-ray optics,⁹ we demonstrate that resonant XRD and differential PDF studies are possible at the *K* edges of elements with *Z* as high as 78 (Pt) and 79 (Au) (*K* edges ~78–81 keV). In particular, we obtain Au-differential PDFs for bulk Cu₃Au alloys which are a typical example of a crystalline material that may show a limited length of structural coherence due to the presence of chemical disorder.¹⁰ The differential PDFs show very good sensitivity to the different ways Au atoms are known to occupy the sites of otherwise identical cubic lattices of those materials, confirming the feasibility of high-energy resonant XRD and differential PDFs studies. Next we study a much more complex system: PtPd

alloy and core-shell nanosized particles developed for catalytic applications.^{11,12} The Pt-differential PDFs we obtain reveal how the atomic ordering of catalytically active Pt atoms is affected by the particular nanoparticles' design. We argue that structural data of such chemical and spatial sensitivity can be invaluable for understanding the properties of complex materials with a reduced length of structural coherence, such as those of PtPd nanosized catalysts.

II. EXPERIMENTAL SECTION

A. Sample preparation

Chemically ordered and disordered Cu₃Au alloys were obtained from the same master alloy prepared by melting of 99.999% Cu and Au under vacuum. The alloy was homogenized by annealing for 3 h at 1200 K. An ingot of the annealed master alloy was rapidly quenched down to room temperature resulting in chemically disordered Cu₃Au. Another ingot was slowly cooled down and allowed to anneal for two weeks at 713 K. This allowed the material to reach a chemically ordered state. Both samples were pulverized, carefully packed between Kapton foils to avoid texture formation and subjected to XRD experiments in transmission geometry.

Monometallic Pd and Pt NPs were prepared via a polyol method¹³ using polyvinylpyrrolidone (PVP, MW = 40,000 g/mol) and degassed ethylene glycol. Core-shell PtPd (50:50) NPs were synthesized using the "sacrificial hydrogen layer" method developed by Toshima *et al.*¹⁴ Following this method, premade monometallic Pd and Pt NPs dissolved in ethanol were coated with hydrogen and then exposed to the secondary metal ions (either Pt²⁺ or Pd²⁺) to create a shell-like coverage. The reaction was done at room temperature. Random alloy PtPd (50:50) NPs were synthesized by a coreduction in H₂PtCl₆ and PdCl₂ refluxed in degassed ethylene glycol in the presence of PVP. Electron microscopy (HAADF-STEM) studies showed that as synthesized NPs were mostly spherical in shape and with narrow-size distributions centered at about 2.4(4) nm for the monometallic and random alloy NPs, and at about 3.5(5) nm for the core-shell NPs. Note since premade 2.4(4) monometallic NPs were used as cores in 3.5(5) core-shell NPs the shells of the latter are indeed only three-atomic-layers thick. More details of the preparation procedures and NP's morphology characterization can be found in Sanchez *et al.*¹⁵ The as prepared NPs, dissolved in ethanol, were sealed in glass capillaries and subjected to XRD experiments.

B. Resonant XRD experiments

Resonant XRD experiments were carried out at the 1-ID beamline of the Advanced Photon Source at Argonne National Laboratory. Ordered and disordered Cu₃Au alloys were measured with x-rays of energy 80.700 and 80.400 keV, i.e., 25 and 325 eV below the Au *K* edge. PtPd NPs were measured with x-rays of energy 78.372 and 78.072 keV, i.e., 23 and 323 eV below the Pt *K* edge. The beam was delivered by a combination of a bent double-Laue premonochromator, collimating refractive lenses, and a four-crystal

high-energy resolution ($\Delta E \sim 8$ eV) monochromator.⁹ The monochromator was calibrated and occasionally checked during data collection for stability against sub-eV energy drifts using the *K* absorption edges of pure Au or Pt foils in transmission. Scattered x-rays were collected by a single, intrinsic Ge detector coupled to a multichannel analyzer. Few energy windows, covering several neighboring channels, were set up to obtain counts integrated over specific energy ranges during the data collection. These energy windows covered: the elastic/coherent intensity only; the elastic, inelastic/incoherent (Compton), and (Au/Pt)*K*_β fluorescence intensities all together; the (Au/Pt)*K*_α fluorescence; and the total intensity scattered into the Ge detector. Integrated counts within these ranges were collected several times scanning up to wave vectors of 25 Å⁻¹ and then averaged to improve the statistical accuracy.¹⁶ The XRD data were corrected for detector dead time, inelastic and background scattering, sample absorption, and resonant Raman fluorescence.

C. Resonant XRD data analysis

The imprecisely known real f' and imaginary f'' dispersion corrections for the resonant atoms were determined in the following way: Au and Pt absorption was measured by scanning across the Au and Pt edges, respectively. These data were scaled to match to the theoretical f'' estimates of Chantler¹⁷ away from the edge to obtain an extended f'' spectrum in absolute units. Then f' was computed from f'' via the Kramers-Kronig relation¹⁷

$$f'(E) = (2/\pi)\mathbf{P} \int \frac{E_i f''(E_i)}{E^2 - E_i^2} dE_i, \quad (1)$$

where \mathbf{P} denotes the Cauchy principal value. The dispersion corrections for Au and Pt resulting from these procedures are shown in Fig. 1. The values for f' and f'' obtained and used are: $f'(\text{Au}) = -7.3$ and $f''(\text{Au}) = 0.70$ at $E = 80.700$ keV; $f'(\text{Au}) = -4.6$ and $f''(\text{Au}) = 0.64$ at $E = 80.400$ keV; $f'(\text{Pt}) = -7.4$ and $f''(\text{Pt}) = 0.69$ at $E = 78.372$ keV; and $f'(\text{Pt}) = -4.7$ and $f''(\text{Pt}) = 0.65$ at $E = 78.072$ keV. The coherent part of XRD data obtained at a given energy was reduced to the so-called total structure function $S(q)$, defined as¹⁸

$$S(q) = \frac{I^{\text{coh}}(q) - [\langle f^2(q) \rangle - \langle f(q) \rangle^2]}{\langle f(q) \rangle^2} = \frac{I^{\text{coh}}(q) - \langle f^2(q) \rangle}{\langle f(q) \rangle^2} + 1, \quad (2)$$

where $I^{\text{coh}}(q)$ is the elastic scattering per atom in electron units and $f(q)$ is the atomic-scattering factor. Note that the atomic-scattering factor is a function both of the wave vector q and x-ray energy E , i.e., $f(q) = f_o(q) + f'(q, E) + if''(q, E)$. The stoichiometric average short notations $\langle f^2(q) \rangle$ and $\langle f(q) \rangle^2$ stand for $\langle f(q)f^*(q) \rangle$ and $\langle f(q) \rangle \langle f^*(q) \rangle$, respectively, and $f^*(q)$ is the complex conjugate of $f(q)$. The wave vector q is defined as $q = 4\pi \sin(\theta)/\lambda$, where θ is half of the scattering angle and λ is the wavelength of the x-rays used. The corresponding total atomic PDFs were obtained via a Fourier transformation as follows:¹⁸

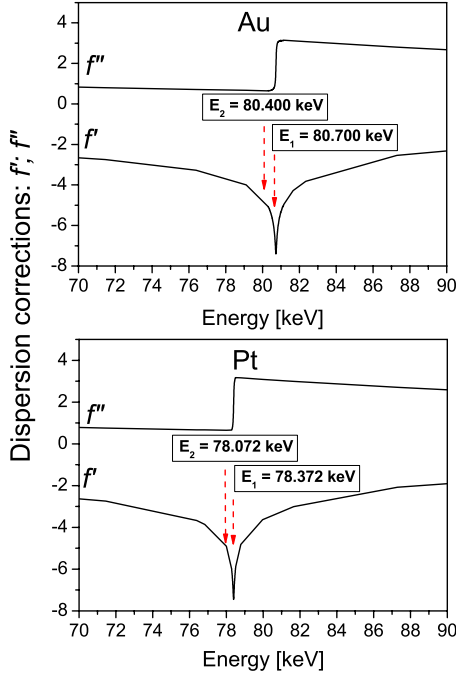


FIG. 1. (Color online) Energy dependence of the real f' and imaginary f'' dispersion corrections for Au and Pt. f' was calculated from the measured f'' values via the Kramers-Kronig relation. The energies below the Au and Pt K edges used in the present experiments are marked with arrows.

$$G(r) = \frac{2}{\pi} \int_{q=0}^{q_{\max}} q[S(q) - 1] \sin(qr) dq, \quad (3)$$

where q_{\max} extends to 25 \AA^{-1} . Note that for a material comprising n atomic species, $G(r)$ is a weighted sum of $n(n+1)/2$ partial PDFs $G_{ij}(r)$, i.e.,

$$G(r) = \sum_{i,j} w_{ij} G_{ij}(r). \quad (4)$$

Here w_{ij} are weighting factors depending on the concentration c_i and scattering power of the atomic species as follows:

$$w_{ij} = c_i c_j \text{Re}[f_i(q) f_j^*(q) / \langle f(q) \rangle^2]. \quad (5)$$

The coherent parts of the XRD data sets obtained at two energies (E_1 and E_2) below the absorption edge of atomic species A ($A = \text{Au}$ or Pt) were used to compute the so-called differential structure functions, $DS(q)_A$, defined as^{5,6,19}

$$DS(q)_A = \frac{I^{\text{coh}}(q, E_1) - I^{\text{coh}}(q, E_2) - [\langle f^2(E_1) \rangle - \langle f^2(E_2) \rangle]}{\langle f(E_1) \rangle^2 - \langle f(E_2) \rangle^2} + 1. \quad (6)$$

The corresponding differential atomic PDFs, $DG(r)_A$, were obtained via a Fourier transformation as follows:

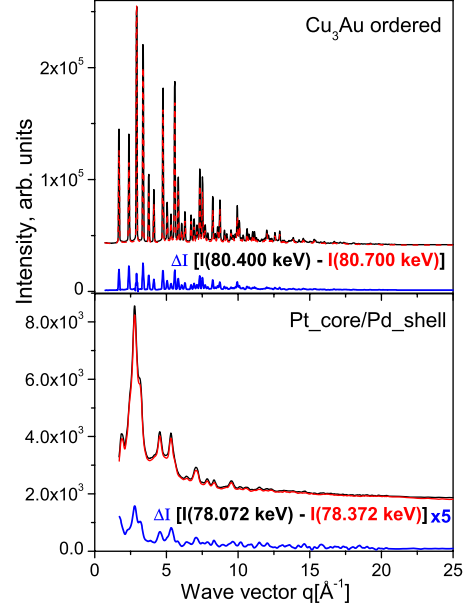


FIG. 2. (Color online) Experimental XRD patterns for ordered Cu_3Au alloys and $\text{Pt}_{\text{core}}/\text{Pd}_{\text{shell}}$ NPs measured with x-rays of two different energies (black and red). The difference ΔI (in blue) between the respective data sets is shown at the lower part of each of the plots. Note ΔI for the NPs is multiplied by a factor of 5 for clarity.

$$DG(r)_A = \frac{2}{\pi} \int_{q=0}^{q_{\max}} q[DS(q)_A - 1] \sin(qr) dq, \quad (7)$$

where q_{\max} extends to 25 \AA^{-1} . Note, since only the scattering form factor of atom A changes significantly, the differential atomic PDFs contain contributions from atomic pairs involving A - i -type atoms only, i.e.,

$$DG(r)_A = \sum_i \Delta w_{Ai} G_{Ai}(r), \quad (8)$$

where

$$\Delta w_{A,i \neq A} = \frac{2c_A c_i \text{Re}[f_i f_A^*(E_1) - f_A^*(E_2)]}{\langle f(E_1) \rangle^2 - \langle f(E_2) \rangle^2}$$

and

$$\Delta w_{AA} = \frac{c_A^2 [f_A^2(E_1) - f_A^2(E_2)]}{\langle f(E_1) \rangle^2 - \langle f(E_2) \rangle^2}. \quad (9)$$

III. RESULTS

As an example, experimental XRD patterns for ordered Cu_3Au alloys and $\text{Pt}_{\text{core}}/\text{Pd}_{\text{shell}}$ nanoparticles are shown in Fig. 2. The XRD data for Cu_3Au alloys show many sharp Bragg peaks which is the typical picture seen with bulk crystalline materials.¹⁰

The patterns for NPs shows only broad diffraction features as usually seen with materials structured at the nanoscale.^{20,21} As can be seen in the figure, the differences, ΔI , between two data sets measured at two different energies

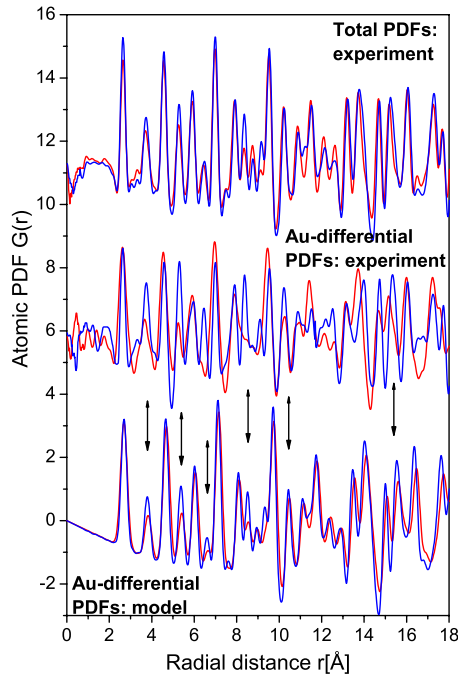


FIG. 3. (Color online) Atomic PDFs for chemically ordered (blue) and disordered (red) Cu_3Au bulk alloys. Arrows mark PDF peaks (second, fourth, sixth, ninth, etc) that differ most for the two different types of atomic arrangement. Note the oscillatory features in the experimental PDFs below 2 Å are unphysical ripples due to XRD data noise and other experimental artifacts that are known to pile up at very low- r values (Refs. 2 and 18).

are small but, as shown below, substantial, and when processed in a rigorous way yield unambiguous, element sensitive structure knowledge. In particular, the total and differential atomic PDFs shown in this work were obtained as follows: diffraction data measured at a given (single) energy, after due corrections, were converted to total structure factors [see Eq. (2)] and then to total atomic PDFs [see Eq. (3)]. The differences, ΔI , between XRD data sets measured at two different energies, after due corrections, were converted to differential structure factors [see Eq. (6)] and then to differential atomic PDFs [see Eq. (7)]. Thus obtained total and Au-differential PDFs for ordered and disordered Cu_3Au alloys are shown in Fig. 3. The total PDFs reflect the correlations between Cu-Cu ($w_{\text{Cu-Cu}}=28\%$), Au-Au ($w_{\text{Au-Au}}=23\%$), and Au-Cu ($2w_{\text{Au-Cu}}=49\%$) atomic pairs in Cu_3Au , while Au-differential PDFs those of Au- i , i.e., Au-Au and Au-Cu atomic pairs only. As can be seen in the figure, the total and Au-differential PDFs for chemically ordered and disordered Cu_3Au exhibit a series of sharp, well-resolved peaks as expected for bulk crystalline materials. The peaks in the PDFs for both alloys are in nearly the same positions since Cu and Au atoms occupy very similar cubic lattices (see Fig. 4, upper part). In ordered Cu_3Au , Cu and Au atoms occupy the face centers and corners, respectively, of a cell [$a=3.75(1)$ Å] of a cubic lattice with space-group symmetry $Pm-3m$. In disordered Cu_3Au alloy, Cu and Au atoms occupy the same lattice [$a=3.76(1)$ Å] positions in a more or less random manner rendering the average crystal symmetry $Fm-3m$.¹⁰ The intensities of the corresponding peaks in

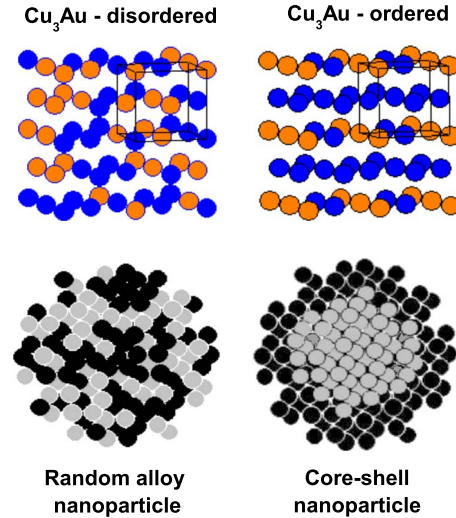


FIG. 4. (Color online) Fragments from the cubic lattices in disordered (S.G. $Fm-3m$) and ordered (S.G. $Pm-3m$) Cu_3Au alloys (Cu-blue, Au-yellow). Cartoons of random alloy and core-shell binary NPs pertaining to PtPd samples studied here are shown as well (lower part).

the experimental PDFs for disordered and ordered Cu_3Au are, however, different, and those differences are beyond the limits of the experimental uncertainty as discussed in Proffen *et al.*¹⁰ The differences come from the fact that the corresponding coordination spheres in ordered and disordered Cu_3Au are occupied by different amounts of Cu and Au atoms and that the atomic-scattering factors of Cu and Au are substantially different. The intensity differences are in line with predictions based on the well-known crystal structures of ordered and disordered Cu_3Au (see the pairs of PDF peaks marked with arrows in Fig. 3) proving the ability of high-energy resonant XRD to reveal accurately fine features of the atomic ordering in materials. As can also be seen in Fig. 3, the differences in the intensities of the second, fourth, sixth, ninth, etc. differential PDF peaks, i.e., the differences between the second, fourth, sixth, ninth, etc. atomic coordination spheres in ordered and disordered Cu_3Au are expressed better in the experimental than in the model-predicted data. This is not a surprise since the predictions are based on data for the “average” crystal structures determined by traditional (Bragg) XRD while the experimental PDF data take into account both the Bragg-type and diffuse components of the XRD data and so reflect the actual local atomic ordering. Furthermore, the differences between the ordered and disordered Cu_3Au structures are seen more clearly in the differential PDFs as compared to those in the total PDF data (Fig. 3). This is a vivid demonstration of the enhanced sensitivity to the atomic-scale structure high-energy resonant XRD delivers by highlighting particular atomic-pair correlations only. Note that if the experiment were done at the L_{III} absorption edge of Au, i.e., with x-rays of energy ~ 11.9 keV, resonant XRD diffraction data could be collected up to $q_{\text{max}} \approx 10$ Å⁻¹ only. The resulting Au-differential PDF would then have had much stronger Fourier termination ripples and worse real-space resolution as can be seen in Fig. 5. Such experimental artifacts distort the profile of experimental

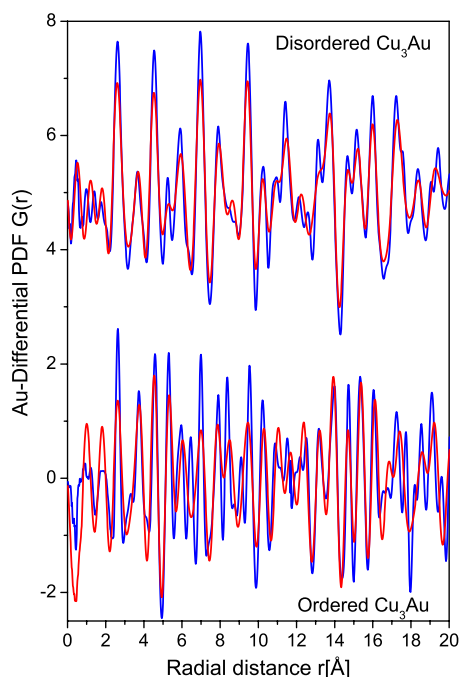


FIG. 5. (Color online) Comparison between experimental Au-differential PDFs for disordered (upper part) and ordered (lower part) Cu_3Au alloys. Data in red correspond to $q_{\text{max}}=10 \text{ \AA}^{-1}$ and data in blue to $q_{\text{max}}=25 \text{ \AA}^{-1}$. Note the differential PDFs derived from diffraction data with a higher q_{max} show weaker spurious features (e.g., see the region from $r=0$ to 2 \AA) and much better resolution (e.g., see the region from $r=6 \text{ \AA}$ to 8 \AA) than those derived from diffraction data with a lower q_{max} .

PDFs and should be avoided since they may severely impair their ability²² to reveal fine features of the atomic ordering and morphology of materials. Obviously resonant XRD aiming at differential PDFs analysis is exploited best when conducted at K rather than at L edges of atomic species, i.e., with x-rays of higher energy. Experimental total PDFs for monometallic Pt ($\sim 2.4 \text{ nm}$), PtPd alloy ($\sim 2.4 \text{ nm}$), and core-shell ($\sim 3.5 \text{ nm}$) NPs are shown in Fig. 6. The total PDFs for bimetallic NPs reflect the correlations between Pt-Pt ($w_{\text{Pt-Pt}}=40\%$), Pt-Pd ($2w_{\text{Pt-Pd}}=46\%$), and Pd-Pd ($w_{\text{Pd-Pd}}=14\%$) pairs of atoms. Experimental Pt-differential PDFs for PtPd alloy and core-shell NPs (see Fig. 4, lower part for an idea about the difference in the morphology of random alloy and core-shell NPs) are shown in Fig. 7. They reflect the correlations between Pt- i , i.e., Pt-Pt and Pt-Pd, atomic pairs only. As discussed below, these differential PDFs have the necessary real-space spatial resolution and element specificity to reveal the atomic ordering in PtPd NPs in very fine detail.

IV. DISCUSSION

As can be seen in Fig. 6, the total PDFs for PtPd NPs show a series of sharp peaks reflecting the presence of well-defined atomic coordination spheres in those materials. These PDFs, however, decay to zero much faster than the PDFs for bulk Cu_3Au alloys, reflecting the much shorter

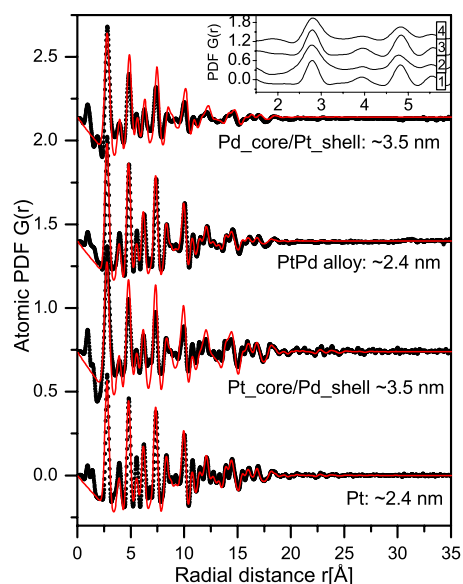


FIG. 6. (Color online) Experimental (symbols) and model (lines in red) total PDFs for PtPd nanosized particles. The models are based on continuous fcc-type lattices. The low- r part of the experimental PDFs (1=pure Pt, 2=Pt_core/Pd_shell, 3=PtPd alloy, and 4=Pd_core/Pt_shell) is given in the inset on an enlarged scale. Note the peaklike features in the experimental PDFs below 2 \AA are unphysical ripples due to XRD data noise and other experimental artifacts that are known to pile up at very low- r values (Refs. 2 and 18).

length of structural coherence in the NPs. The experimental PDF for pure Pt NPs has its first peak positioned at $2.76(2) \text{ \AA}$ which is the Pt-Pt distance in bulk Pt metal. Also, that PDF may be approximated very well with a model featuring a continuous fcc-type lattice with very little structural disorder. In this type of models a PDF for an infinite lattice is first computed and then multiplied by a particle shape- (spherical in our case) dependent function which is zero for distances longer than the size of the NP being modeled.²³ The computations were done with the help of the program PDFGUI.²⁴ It is a simplistic approximation to the structure of real NPs but is useful since it allows to determine the type of atomic ordering in NPs and obtain a set of structural parameters (e.g., lattice constants) that may be compared directly with those for the corresponding bulk materials. Thus obtained “lattice” parameter for pure Pt NPs is $a=3.925(1) \text{ \AA}$. For reference the lattice parameter of bulk fcc Pt is $a=3.924(1) \text{ \AA}$. This result shows that pure Pt NPs may well be viewed as nanosized pieces of bulk Pt, i.e., that atoms inside Pt NPs sit on the vertices of a $2.4(4) \text{ nm}$ piece of a continuous fcc-type lattice. HAADF-STEM studies of Pt NPs of the same series studied here (see Fig. 1a in Ref. 15) show the same. The total PDF for PtPd alloy NPs may also be approximated very well by a model featuring a 2.4-nm piece of a continuous fcc-type lattice whose vertices are occupied by Pt and Pd atoms arranged in a random manner. The result is in line with the findings of HAADF-STEM (see Fig. 5 in Ref. 15). A model based on a continuous fcc lattice, however, is less successful in approximating the total PDFs for core-shell NPs, indicating that the atomic ordering in

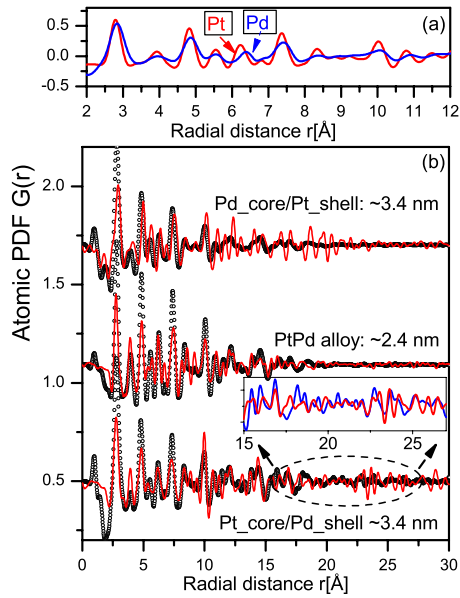


FIG. 7. (Color online) Experimental total PDFs for pure Pt (in red) and Pd (in blue) NPs (a). Experimental total (symbols) and Pt-differential (lines in red) PDFs for PtPd NPs (b). The higher- r part of Pt differential PDF for Pt_core/Pd_shell particles is compared with a model one (line in blue) for an fcc-type structure in the inset. The oscillatory behavior of the model and experimental data agree showing that the higher- r peaks in the differential PDFs are structure relevant features and not data noise. Note the peaklike features in the experimental PDFs below 2 Å are unphysical ripples due to XRD data noise and other experimental artifacts that are known to pile up at very low- r values (Refs. 2 and 18).

core shell and alloy PtPd NPs studied here is of the same fcc type but yet fairly different. The origin of this difference may be surmised from the behavior of the experimental total PDFs. The total PDFs for pure Pt and PtPd alloy NPs show physical oscillations up to interatomic distances of ~ 2 nm which is close to the average NP's size of 2.4(4) nm. So it is the size of NP's that mostly determines the length of structural coherence in pure Pt and PtPd alloy NPs. The total PDFs for core-shell NPs, that are approx. 3.5(5) nm in size, also decay to zero by distances ~ 2 nm. Hence, the atomic ordering in core-shell NPs is influenced by an additional effect that reduces their length of structural coherence well beyond the effect associated with finite size/surface-relaxation effects.^{20,21} This additional effect is seen as an extra broadening of all atomic coordination spheres in the core-shell NPs as compared to those in pure Pt and PtPd alloy NPs (see the extra broadening of the PDFs for core-shell NPs shown in the inset in Fig. 6). Better understanding of this extra, atomic disorder-type effect can be obtained by analyzing the experimental differential PDFs as demonstrated below.

As can be seen in Fig. 7 the first peak in the Pt-differential PDFs for PtPd alloy and Pt_core/Pd_shell NPs is positioned at 2.76(2) Å and has a quite sharp full-width at half maximum (FWHM) ~ 0.3 Å. The first peak in the total PDF for pure Pt NPs has virtually the same position and FWHM. Furthermore, the peaks in the Pt-differential PDFs for

Pt_core/Pd_shell NPs follow a pattern typical for an fcc-type packing of atoms [see the inset in Fig. 7(b)] up to interatomic distances of ~ 3 nm, which are close to the average NP's size (~ 3.4 nm). All these results show that Pt atoms pack closely [Pt-Pt separation $\sim 2.76(2)$ Å] and in an fcc-type pattern in pure Pt, PtPd alloy, and Pt_core/Pd_shell NPs, as they do in bulk Pt. When Pd atoms are alloyed with Pt the fcc-type packing of the latter is hardly disturbed as demonstrated by the very similar behavior of the total and Pt-differential PDFs for PtPd alloy NPs [see Fig. 7(b)]. As a result, PtPd alloy NPs show little structural disorder, the atomic coordination spheres/PDF peaks are sharp, and the length of structural coherence, just like that in pure Pt NPs, is set by the NP's size. Other studies have also found that the packing of the heavier of the two atomic species involved in binary metallic alloys usually dominates their atomic-scale structure.²⁵

However, when Pd atoms are not alloyed with Pt but deposited as a shell they seem to form a rather loose packing that is not well lined up with that of the core. Indeed, as the data in Fig. 7(a) show, the first neighbor distance in pure Pd NPs is longer [$\sim 2.86(2)$ Å] than that in pure Pt [$\sim 2.76(2)$ Å] NPs. For reference, Pd-Pd distance in bulk Pd is ~ 2.74 Å. The degree of structural disorder in Pd NPs, measured by the FWHM of the first PDF peak, is also larger (~ 0.5 Å) than that (~ 0.3 Å) in Pt NP. Also HAADF-STEM studies show pure Pd NPs to be much less ordered at the atomic scale than pure Pt NPs [see Fig. 1b in Ref. 15]. As a result the consecutive coordination spheres in pure Pt and Pd NPs are not well-lined up with each other [see the arrows in Fig. 7(a)]. Obviously the premade Pt core and the subsequently deposited Pd shell of Pt-core/Pd-shell NPs studied here maintain the atomic ordering of the respective monometallic NPs. The atomic coordination spheres in the 2.4(4) nm Pt core and three Pd atomic-layer shell thus remain “out-of-phase,” and hence, the total PDF decays to zero at distances shorter than the NP's size. A similar picture is observed with Pd_core/Pt_shell NPs. Here the total PDF also decays to zero at distances less than but comparable to the core diameter (see Fig. 6) and the corresponding Pt-differential PDF shows physical oscillations to considerably longer distances [Fig. 7(b)]. In addition, the first peaks in the total [2.80(2) Å] and differential PDFs [2.88(2) Å] are considerably shifted with respect to each other. Obviously, when deposited as a three-atomic-layer shell, Pt atoms do not pack as densely as in pure Pt NPs nor they line up with the Pd core, i.e., the Pd core and Pt shell are not well-lined up with respect to each other. Note that HAADF-STEM studies too conclude that the atomic ordering in Pt_core/Pd_shell NPs is quite complex and of a phase-segregated type.¹⁵

The findings here thus show that using a “sacrificial” hydrogen layer to deposit thin shells on premade cores not only prevents Pt and Pd atoms from alloying each other but apparently keeps the core and shell structurally incoherent. In Pt_core/Pd_shell NPs a densely packed ~ 2.4 -nm Pt core is surrounded by a shell of somewhat loosely packed Pd atoms; in Pd_core/Pt_shell NPs a ~ 2.4 -nm core of loosely and quite irregularly packed Pd atoms is covered by a somewhat loose shell of Pt atoms. Accordingly, Pt_core/Pd_shell

and Pd_core/Pt_shell NPs develop fine but substantial structural differences. The differences are reflected in the total PDFs (see Fig. 6) but unambiguously discriminated by the Pt-differential PDFs only [Fig. 7(b)]. Structurally incoherent shells are known to improve the efficiency of semiconductor NPs (quantum dots).²⁶ How such shells would affect the catalytic properties of PtPd NPs is yet to be seen. As to the disorder in Pd NPs/cores, it is likely to be caused by a strong surface relaxation effect introduced by the capping layer of PVP molecules. That capping layer obviously does not influence Pt NPs/cores much since Pt($Z=78$) is much heavier than Pd($Z=46$). The disorder/loose packing in the NPs shells may be due to hydrogen atoms from the “sacrificial” layer that embed into them.²⁷ Indeed, structural disorder may occur easily in shells that are only few (three in our case) atomic layers thick.

V. CONCLUSIONS

By conducting successful high-energy resonant XRD and differential atomic PDFs studies on chemically ordered and disordered Cu₃Au alloys with a well-known structure we prove in practice that this experimental approach can reveal the atomic ordering in materials of limited structural coherence with very good spatial resolution and element specificity. By probing the K edge of Pt atoms in nanosized alloy and core-shell PtPd particles we show that they exhibit a great deal of structural diversity reflecting the different way Pt and Pd assemble at the nanoscale. The resonant XRD-based results agree with those of HDAAF-STEM experiments but go beyond the mostly qualitative picture yielded by imaging techniques by providing a firm, quantitative basis for a rigorous modeling of the three-dimensional atomic ordering in the nanoparticles. Such models are a critical prerequisite to understanding the NP’s properties, in particular, the catalytic

one. Structural models based on continuous lattices with little structural disorder may suffice in the case of pure Pt and PtPd alloy NPs. However, more precise models that incorporate substantial disorder and feature structurally incoherent cores and shells should be constructed and used for the core-shell PtPd NPs. A possible approach is to employ reverse Monte Carlo (RMC) simulations that are capable of handling larger-size atomic configurations followed by density-functional or molecular-dynamics simulations to achieve an energy minimization and uniqueness of the RMC model solution as demonstrated in Ref. 20. Also, the finite size of NPs should be taken into account explicitly²⁸ and not just approximated.²³ Experimental Pt-differential PDFs, as obtained here, will be indispensable in guiding such modeling studies.

On a more general note, nanosized materials based on Au and Pt are also being explored for high magnetic-density recording, bio-imaging, and drug delivery. These research areas can also benefit significantly from high-energy resonant XRD coupled to differential atomic PDF data analysis. In general, structure data of excellent spatial resolution and element specificity can be obtained for any material of limited structural coherence that contains elements with a K -absorption edge of ~ 20 keV or higher. Furthermore, the technique requires a small amount of sample and works in various sample environments (e.g., in solution). Given this, and the number of high-energy synchrotron radiation facilities available worldwide, the technique should find widespread utility.

ACKNOWLEDGMENTS

We would like to acknowledge R. G. Nuzzo, S. I. Sanchez, and M. W. Small for providing the PtPd samples and engaging in meaningful discussions. Work at APS is supported by DOE under Contract No. DE-AC02-06CH11357.

*petkov@phy.cmich.edu

¹V. Petkov, S. J. L. Billinge, S. D. Shastri, and B. Himmel, *Phys. Rev. Lett.* **85**, 3436 (2000).

²T. Egami and S. J. L. Billinge, *Underneath the Bragg Peaks* (Pergamon Press, Amsterdam, 2003).

³V. Petkov, *Mater. Today* **11**, 28 (2008).

⁴W. Dmowski, T. Egami, K. E. Swider-Lyons, W.-F. Yan, S. Dai, and S. H. Overbury, *Z. Kristallogr.* **222**, 617 (2007).

⁵P. H. Fuoss, P. Eisenberger, W. K. Warburton, and A. Bienenstock, *Phys. Rev. Lett.* **46**, 1537 (1981); Y. Waseda, *Novel Applications of Anomalous (Resonance) X-Ray Scattering for Characterization of Disordered Materials* (Springer, Berlin, 1984).

⁶J. B. Kortright and A. Bienenstock, *Phys. Rev. B* **37**, 2979 (1988).

⁷To keep to a minimum the experiment-introduced attenuation of the longer-range interatomic correlations/higher- r peaks in experimental atomic PDFs, including differential PDFs, a detector with a good spatial resolution, e.g., a point detector, is recommended to be used as in the present work. At the same time, to

keep to a minimum the smearing of the short-range interatomic correlations in experimental atomic PDFs, including differential PDFs, the respective XRD data should be collected to as high wave vectors q_{\max} as possible. The effect of the detector resolution and the finite size of q_{\max} on the experimental PDFs is discussed in more detail in Q. Xiangyun, E. Bozin, P. Juhas, Th. Proffen, and S. J. L. Billinge, *J. Appl. Crystallogr.* **37**, 110 (2004).

⁸V. Petkov, J.-K. Jeong, F. Mohiuddin-Jacobs, Th. Proffen, S. J. L. Billinge, and W. Dmowski, *J. Appl. Phys.* **88**, 665 (2000).

⁹S. D. Shastri, J. Almer, C. Ribbing, and B. Cederström, *J. Synchrotron Radiat.* **14**, 204 (2007).

¹⁰Th. Proffen, V. Petkov, S. J. L. Billinge, and T. Vogt, *Z. Kristallogr.* **217**, 47 (2002).

¹¹H. Li, G. Sun, N. Li, S. Sun, D. Su, and Q. Xin, *J. Phys. Chem. C* **111**, 5605 (2007).

¹²J. Yang, J. Lee, Q. Zhang, W. Zhou, and Z. Liu, *J. Electrochem. Soc.* **155**, B776 (2008).

¹³F. Bonet, K. Tekaia-Elhsissen, and K. V. Sarathy, *Bull. Mater. Sci.* **23**, 165 (2000).

- ¹⁴Y. Wang and N. Toshima, *J. Phys. Chem. B* **101**, 5301 (1997).
- ¹⁵S. I. Sanchez, M. W. Small, J. Zuo, and R. G. Nuzzo, *J. Am. Chem. Soc.* **131**, 8683 (2009).
- ¹⁶Note, we could have collected data up to approximately 40 \AA^{-1} with the as-described experimental set up. However, we did not go to such high wave vectors since (i) no fine, short-range structural features needed to be resolved with the materials studies here and (ii) we had to optimize the experiment with respect to the total data-collection time. For reference, the data collection time for a sample for a given energy amounted to about 5 h when data to $q_{\text{max}}=25 \text{ \AA}^{-1}$ was collected. In future studies this data-collection time can be shortened considerably if a multicrystal Ge detector is employed.
- ¹⁷C. T. Chantler, *J. Phys. Chem. Ref. Data* **24**, 7 (1995).
- ¹⁸C. N. J. Wagner, *J. Non-Cryst. Solids* **31**, 1 (1978).
- ¹⁹R. Serimaa, O. Serimaa and A. Bienenstock, *J. Non-Cryst. Solids* **192-193**, 372 (1995).
- ²⁰V. Petkov, N. Bedford, M. R. Knecht, M. G. Weir, R. M. Crooks, W. Tang, and G. Henkelman, and A. Frenkel, *J. Phys. Chem. C* **112**, 8907 (2008).
- ²¹V. Petkov, *Synchrotron Radiat. News* **22**, 29 (2009).
- ²²V. Petkov, P. D. Cozzoli, R. Buonsanti, R. Cingolani, and Y. Ren, *J. Am. Chem. Soc.* **131**, 14264 (2009).
- ²³K. Kodama, S. Iikubo, T. Taguchi, and S. Shamoto, *Acta Crystallogr.* **62**, 444 (2006); B. Gilbert, *J. Appl. Crystallogr.* **41**, 554 (2008).
- ²⁴C. L. Farrow, P. Juhas, J. W. Liu, D. Bryndin, E. S. Bozin, J. Bloch, Th. Proffen, and S. J. L. Billinge, *J. Phys.: Condens. Matter* **19**, 335219 (2007).
- ²⁵A. I. Frenkel, E. A. Stern, A. Rubshtein, A. Voronel and Yu. Rosenberg, *J. Phys. IV* **7**, C2-1005 (1997).
- ²⁶B. O. Dabbousi, J. Rodriguez-Viejo, F. V. Mikulec, J. R. Heine, H. Mattoussi, R. Ober, K. F. Jensen, and M. G. Bawendi, *J. Phys. Chem. B* **101**, 9463 (1997).
- ²⁷L. C. Witjens, J. H. Bitter, A. J. Dillen, F. M. F. Groot, D. C. Koningsberger, and K. P. Jong, *Phys. Scr.* **T115**, 278 (2005).
- ²⁸V. I. Korsunskiy, R. B. Neder, A. Hofmann, S. Dembski, C. Graf, and E. Rühl, *J. Appl. Crystallogr.* **40**, 975 (2007); R. B. Neder and Th. Proffen, *Diffuse Scattering and Defect Structures* (Oxford University Press, Oxford, 2008), Chap. 9.